OPEN

Core-shell silicon nanowire solar cells

M. M. Adachi[1,2], M. P. Anantram[3] & K. S. Karim[1,2]

[1]Department of Electrical and Computer Engineering, [2]Waterloo Institute for Nanotechnology, University of Waterloo, Waterloo, Ontario N2L 3G1, Canada, [3]Department of Electrical Engineering, University of Washington, Seattle, Washington 98105-2500, USA.

Silicon nanowires can enhance broadband optical absorption and reduce radial carrier collection distances in solar cell devices. Arrays of disordered nanowires grown by vapor-liquid-solid method are attractive because they can be grown on low-cost substrates such as glass, and are large area compatible. Here, we experimentally demonstrate that an array of disordered silicon nanowires surrounded by a thin transparent conductive oxide has both low diffuse and specular reflection with total values as low as < 4% over a broad wavelength range of 400 nm < λ < 650 nm. These anti-reflective properties together with enhanced infrared absorption in the core-shell nanowire facilitates enhancement in external quantum efficiency using two different active shell materials: amorphous silicon and nanocrystalline silicon. As a result, the core-shell nanowire device exhibits a short-circuit current enhancement of 15% with an amorphous Si shell and 26% with a nanocrystalline Si shell compared to their corresponding planar devices.

S olar power, harvested by photovoltaic devices, is an abundant, clean, and renewable energy source. In recent years, nanowires have been investigated for improving optical absorption[1–10] and collection efficiency[11,12] in photovoltaic devices while using less material than planar devices. Bottom up grown nanowires, usually by the vapor-liquid-solid (VLS) method, offer a simple and large area compatible method for synthesizing a dense array of silicon nanowires on low cost glass substrates. This method also facilitates tailoring of the optical properties of the nanowires by independent control of nanowire diameter and length. However, metal catalysts introduced during vapor-liquid-solid (VLS) nanowire growth can significantly degrade carrier collection efficiency[2,13]. A number of attempts have been made to circumvent the effect of catalyst impurities on device performance such as removal of catalyst impurities after nanowire growth by thermal oxidation[14], or surface passivation by an Al_2O_3 film[15]. However, conversion efficiencies of solar cells incorporating bottom-up grown nanowires remain relatively low[1–2,14–18]. Here, we show that disordered Si nanowires surrounded by a thin transparent conductive oxide outer shell exhibit both low broadband diffuse and specular reflectance. Furthermore, core-shell nanowire devices with both an amorphous Si and nanocrystalline Si absorber shell exhibit strong enhancement in external quantum efficiency and short-circuit current compared to planar control devices. All nanowires and thin film Si and electrical contacts are prepared by large-area compatible vacuum processes on glass substrates, making this approach attractive for large-area, low-material cost production.

Si nanowires are incorporated into a core-shell nanowire solar cell as illustrated in Figure 1a. A thin transparent ZnO : Al (average radial thickness = 23 nm) layer coats the nanowires and acts as a barrier for 1) isolating the nanocluster catalyst introduced during nanowire growth from the active n-i-p shell, and 2) preventing counter-doping of the n-type layer by the Al back contact[19]. Therefore, the nanowires are not active device absorbers but rather provide high aspect ratio structure to the active n-i-p shell surrounding the nanowire where photogeneration and collection of photogenerated carriers occurs. Two devices are fabricated, one with an amorphous Si absorber shell and one with a nanocrystalline Si absorber shell. The results of each device are discussed separately. Nanocrystalline Si is a stable thin film material which has an indirect bandgap close to that of crystalline Si (~1.1 eV)[20]. Furthermore, nanocrystalline Si absorbs infrared light, and can therefore be used in a tandem cell configuration with amorphous Si for increasing total broadband absorption. However, like crystalline Si, nanocrystalline Si has an indirect bandgap so light absorption is weak in thin films, particularly at infrared wavelengths. Therefore, a light trapping mechanism is essential for maximizing device performance in nanocrystalline Si devices. The incident light enters the device through a thin ZnO : Al top contact. The planar control cell which has an intrinsic thickness t, as illustrated in Figure 1b, is used for comparison.

Results

Amorphous Si nanowire shell solar cells. A highly dense array of Si nanowires was grown by VLS method on an Al coated glass substrate as shown in the Secondary Electron Microscopy (SEM) image in Figure 2a. The average
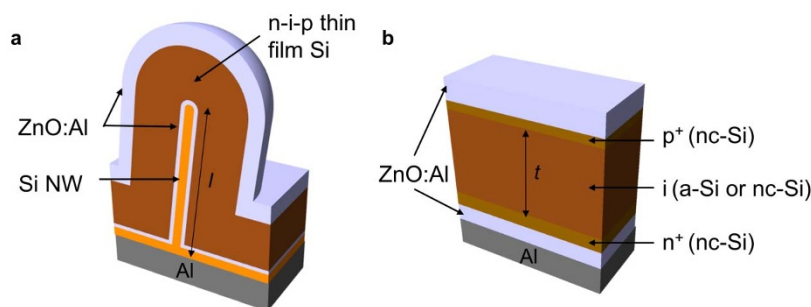
Figure 1 | Core-shell Si nanowire device architecture. (a) 3D cross-section illustration of the core-shell Si nanowire (NW) device structure. The active device region is the radial n-i-p thin film Si shell surrounding the nanowire. Light is incident through the aluminum doped ZnO (ZnO : Al) transparent conductive oxide top contact. The intrinsic (i) region is amorphous Si (a-Si) or nanocrystalline Si (nc-Si). (b) 3D cross-section illustration of a planar control cell.

nanowire length is 525 nm, and the average nanowire diameter is 20 nm. The nanowires after coating by a thin ZnO : Al barrier layer is shown in Figure 2b, and the final device structure consisting of a radial n-i-p shell and ZnO : Al top contact is shown at a 45° tilt-view in Figure 2c and as a cross-section (75° tilt-view) in Figure 2d. The average total diameter of the n-i-p radial nanowire device is 360 nm without top ZnO : Al contact and 440 nm with top ZnO : Al contact. The ZnO : Al top contact has an average thickness of 74 nm at the top of the nanowires (Figure 2d) and thinner along the vertical sidewalls. Due to the higher surface area of the nanowires and thin top contact layer, Ag gridlines were necessary to decrease the series resistance of the top contact.

The total (specular and diffuse) reflectance of a core-shell nanowire a-Si solar cell and a planar a-Si solar cell is shown in Figure 3a. The thickness of the ZnO : Al contact for the planar device was measured to be 75 nm ± 5 nm, chosen to satisfy the quarter-wavelength minimum reflectance condition of $dn = \lambda/4$ for incident light normal to the substrate, where d is the thickness of the film and n is the index of refraction of the antireflective coating (n $\sim$ 2.0 for ZnO : Al)[21]. The total reflectance of the planar device exhibits a minimum of 0.5% at λ = 550 nm, but is much higher at short (37% at λ = 360 nm) and long wavelengths (> 60% for λ > 670 nm). In comparison, the core-shell

NW device structure strongly suppresses broadband reflectance. The total reflectance of the core-shell nanowire structure is < 4% over a broad wavelength interval of 400 nm < λ < 650 nm where absorption in a-Si is most efficient, and exceeds 10% only for λ > 700 nm. Note that the transmission through Al/glass was measured to be zero for the entire spectrum so no light is lost to transmission.

The external quantum efficiency, defined as the percentage of electrons collected per incident photon measured under short-circuit conditions, of the core-shell nanowire solar cell and that of the planar a-Si solar cell is shown in Figure 3b. The nanowire device exhibits higher external quantum efficiency (EQE) than the planar device over most of the wavelength spectrum. The higher EQE can be attributed to lower reflectance losses (Figure 3a) in the nanowire device and enhanced infrared absorption caused by multiple scattering within the nanowire shell. The EQE enhancement ratio between the nanowire device and planar device (i.e., EQE_{NW}/EQE_{planar}) is as high as 3.2 at λ = 700 nm. The core-shell nanowire device has a lower EQE than the planar device only within the wavelength interval λ = 500 nm to 600 nm, which is caused by higher absorption loss in the p$^+$ Si shell in the nanowire device. The nanowire device required a 50% longer p$^+$ Si deposition than in the planar device to sufficiently cover the nanowire side-walls for efficient charge collection leading to higher absorption
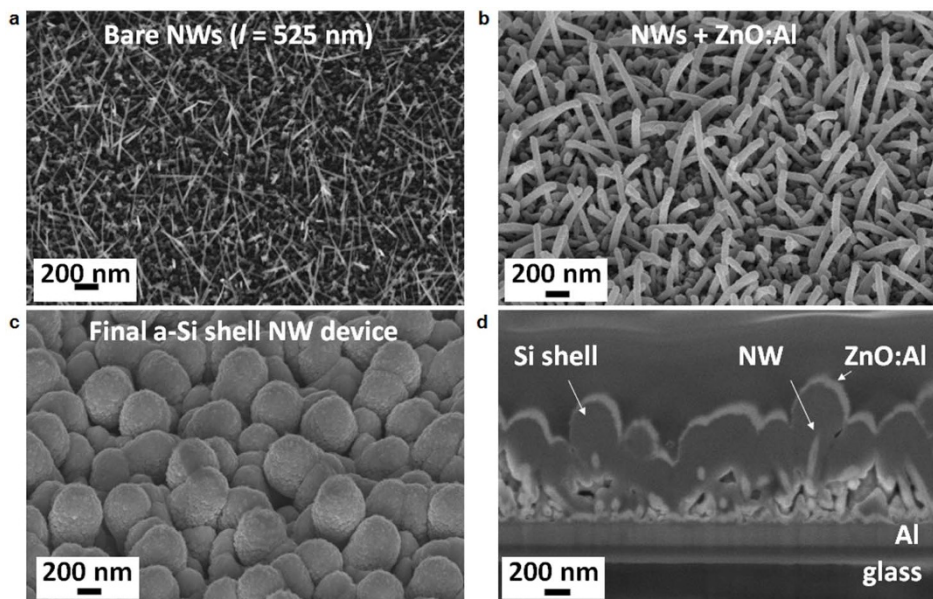

Figure 2 | Amorphous Si nanowire shell solar cells at different stages of fabrication. (a) SEM image (45° tilt) of an array of bare Si nanowires with an average nanowire length of l = 525 nm and average nanowire diameter of 20 nm. (b) SEM image (45° tilt) of an array of nanowires (NWs) surrounded by a thin layer of ZnO : Al (b). (c) SEM image (45° tilt) and (d) cross-sectional SEM (75° tilt) of the final n-i-p radial nanowire solar cell with ZnO : Al top contact. The intrinsic nanowire shell material is amorphous Si and the average diameter of the total device structure is 440 nm with ZnO : Al top contact.
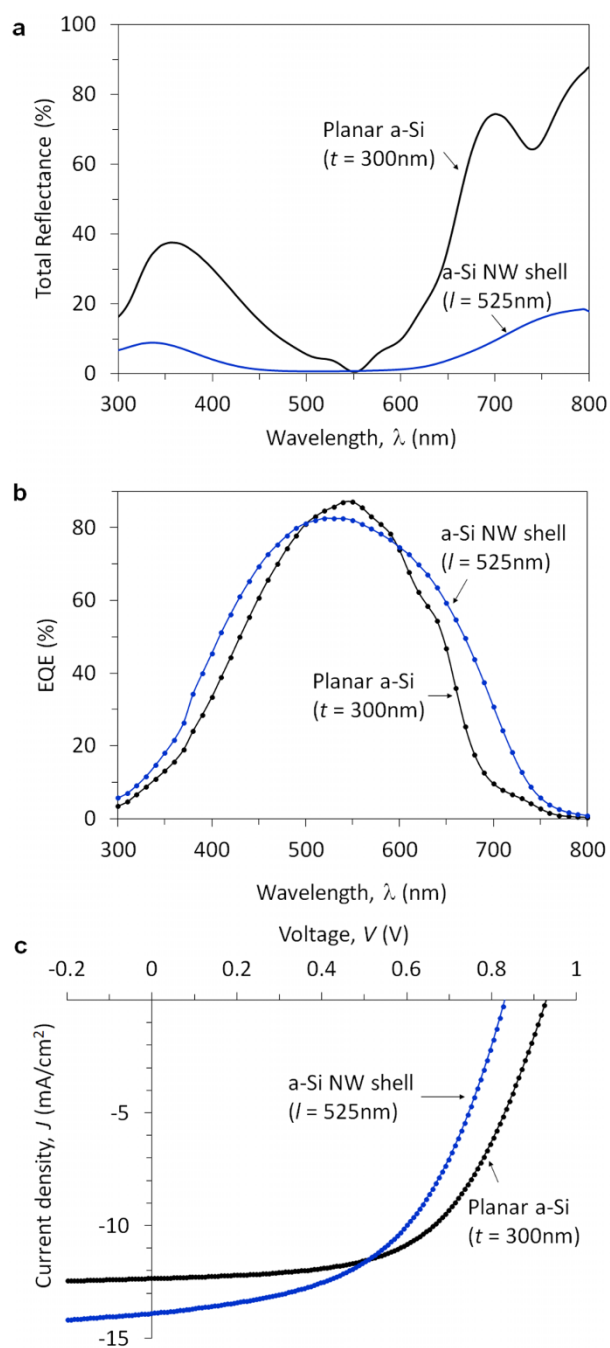
Figure 3 | Performance of amorphous Si nanowire shell solar cells.
(a) Total (specular and diffuse) reflectance of an amorphous Si (a-Si) nanowire (NW) shell solar cell and a planar a-Si control device. The total reflectance of the amorphous Si nanowire shell device is < 4% in the wavelength interval of 400 nm < λ < 650 nm and exceeds 10% only at λ > 700 nm. (b) External quantum efficiency (EQE) spectra at zero voltage bias of the amorphous Si nanowire shell solar cell (average nanowire length l = 525 nm). The nanowire device demonstrates higher EQE than the planar device for all wavelengths other than the interval λ = 500 nm–600 nm. (c) J–V characteristic under AM 1.5 global illumination (100 mW/cm²) of the amorphous Si nanowire shell solar cell. The nanowire device has a J_{sc} = 13.9 mA/cm², V_{oc} = 0.830 V, FF = 52.4%, and conversion efficiency of η = 6.0%. The device characteristics of the planar a-Si device is J_{sc} = 12.1 mA/cm², V_{oc} = 0.932 V, FF = 57.9%, and η = 6.5%.

losses in the p⁺ region than the planar device. One method to increase EQE further is to improve conformal coverage of the p⁺ Si shell around the nanowires, facilitating the use of a thinner p⁺ Si shell.

The current density (J) versus voltage (V) measurements under solar simulator spectrum (AM 1.5 global) illumination of the a-Si nanowire shell device and planar a-Si control device are shown in Figure 3c. The nanowire device has a short circuit current density (J_{sc}) of 13.9 mA/cm², open circuit voltage (V_{oc}) of 0.830 V, fill factor (FF) of 52.4%, and conversion efficiency (η) of 6.0%. In comparison, the device characteristics of the planar a-Si device was J_{sc} = 12.1 mA/cm², V_{oc} = 0.932 V, FF = 57.9%, and η = 6.5%. The short circuit current in the nanowire device corresponds to a 15% improvement than that of the planar device. The J_{sc} measured by J-V measurements agree to within 3% with the J_{sc} determined from the integrated EQE spectra in Figure 3b, thus verifying the calibration of the measurement. Further discussion on the device performance of the nanowire device is presented in the Discussion section.

Nanocrystalline Si nanowire shell solar cells. The device architecture of the nanocrystalline Si nanowire shell device is the same as that of the amorphous Si nanowire shell device (Figure 1a). Arrays of two different average nanowire lengths, l = 525 nm and 800 nm, are incorporated into core-shell devices. The average diameter (with ZnO : Al contact) of the nanowire tip is 574 nm for l = 525 nm, and 533 nm for l = 800 nm (Supp. Figure S3d).

The total reflectance spectra of nanocrystalline Si nanowire shell solar cells with two different average nanowire lengths of 525 nm and 800 nm, and that of a planar nanocrystalline Si solar cell are shown in Figure 4a. The planar nanocrystalline Si device shows high total reflectance with values of up to 24% at a short wavelength of λ = 350 nm and exceeds 40% for λ > 700 nm. In comparison, the total reflectance of both nanowire devices is ≤ 6% over the wavelength range of λ = 400 nm to 650 nm which is slightly higher than that of the amorphous Si shell reflectance in Figure 3a. The higher reflectance of the nanocrystalline Si nanowire shell devices can be attributed to less spacing between nanowires for the nanocrystalline Si shell device. More specifically, for the same average nanowire length (l = 525 nm), the average diameter of the nanocrystalline Si shell and amorphous Si shell devices without a top contact was 475 nm and 360 nm, respectively. The reflectance of the nanocrystalline Si nanowire shell devices exceeds 10% only for λ > 700 nm at which absorption in nanocrystalline Si is weak.

The external quantum efficiency spectra of nanocrystalline Si nanowire shell solar cells with an average length of 525 nm and 800 nm are shown in Figure 4b. The EQE of a planar solar cell consisting of a 1 μm nanocrystalline Si intrinsic layer is also shown for comparison. Both core-shell nanowire devices exhibit higher EQE than the planar device over nearly the entire wavelength spectrum (λ = 300–1000 nm). Furthermore, the core-shell nanowire devices with a longer nanowire length (l = 800 nm) exhibit higher EQE than that of the shorter nanowire length (l = 525 nm) over all wavelengths, particularly at longer wavelengths between 500–900 nm.

The J-V curves of nanocrystalline Si nanowire shell solar cells with lengths of 525 nm and 800 nm under AM 1.5 global illumination (100 mW/cm²) are shown in Figure 4c. The J–V curve of the planar nanocrystalline Si solar cell with an intrinsic nanocrystalline Si layer thickness of 1 μm is shown for reference for which J_{sc} = 13.2 mA/cm², FF = 54.8%, V_{oc} = 0.42 V, and η = 3.0%. Both nanocrystalline Si nanowire shell solar cells show strong improvement in J_{sc}, with respect to the planar device: 14.9 mA/cm² for l = 525 nm and 16.6 mA/cm² for l = 800 nm. These values correspond to an enhancement in J_{sc} of 13% and 26%, respectively. The other device parameters of the shorter nanocrystalline Si nanowire (l = 525 nm) shell solar cell are V_{oc} = 0.39 V and FF = 50.3%, resulting in a conversion efficiency of η = 2.9%. For the longer nanocrystalline Si nanowire shell device (l = 800 nm), V_{oc} = 0.37 V, FF = 38.0%, and η = 2.3%.
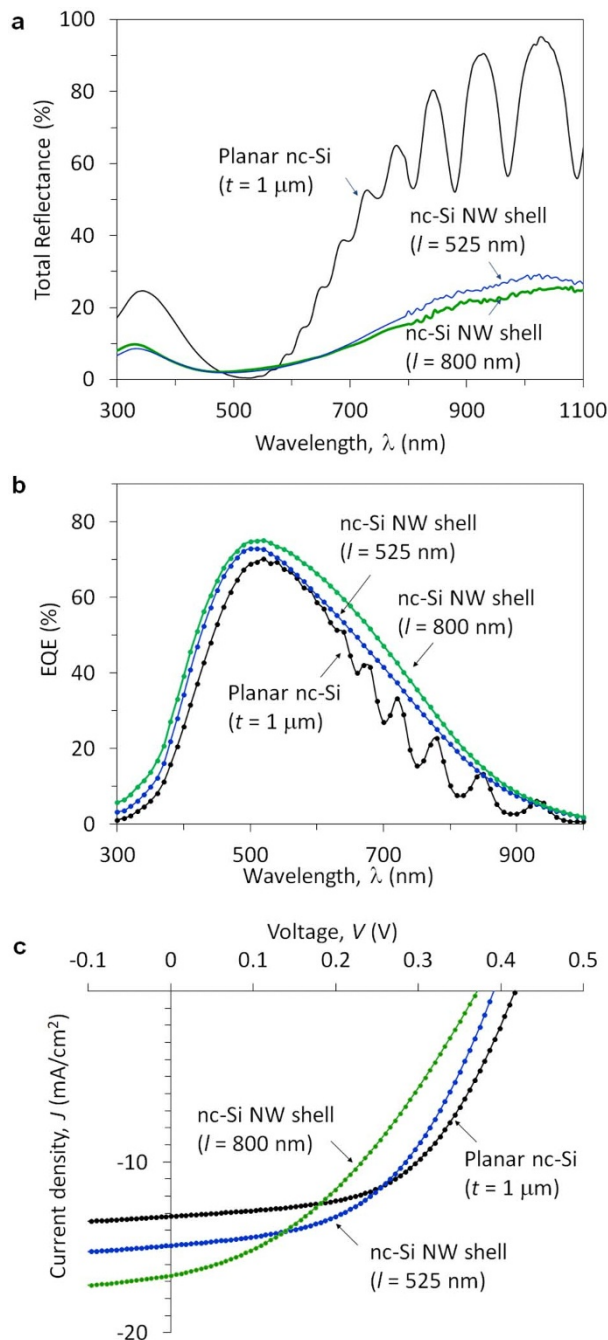
Figure 4 | Performance of nanocrystalline Si nanowire shell solar cells.
(a) Total (specular and diffuse) reflectance of nanocrystalline Si (nc-Si) nanowire (NW) shell solar cells with an average nanowire length l of 525 nm and 800 nm, and a planar nc-Si control device. (b) External quantum efficiency (EQE) spectra of the nanocrystalline Si nanowire shell solar cells. The core-shell solar cell with the longest nanowires (l = 800 nm) demonstrates the highest quantum efficiency at nearly all wavelengths (λ = 300 to 1000 nm). (c) J–V curves under AM 1.5 global illumination (100 mW/cm²) of the nanocrystalline Si nanowire shell solar cells.

Discussion

Figure 3a and 4a shows the total reflectance of core-shell nanowire solar cells with two different shell materials, amorphous Si and nano-crystalline Si, respectively. One of the drawbacks of bare disordered nanowires is that they have high diffuse reflectance at high photon energies (e.g. 33% at 2.2 eV) due to diffuse light scattering [8]. The

total reflectance spectra in Figure 3a and 4a experimentally demonstrates that low diffuse reflectance can be achieved in disordered Si nanowires when coated with a suitably thin transparent oxide layer. The ZnO : Al shell acts as an anti-reflective coating with an intermediate refractive index between that of air and Si (n ∼ 2 for ZnO : Al), reducing diffuse light scattering by the nanowires. In fact, a theoretical study of a single core-shell nanowire consisting of an amorphous Si nanowire coated with a thin dielectric has shown that this core-shell structure can lead to significant absorption enhancement compared to an amorphous Si nanowire on its own[22]. The oxide shell acts as an anti-reflective coating with optimal anti-reflective properties when the thickness of this layer is 70 nm. In our study, the ZnO : Al thickness at the top of core-shell nanowires is measured to be on average 74 nm facilitating the low reflectance observed in Figures 3a and 4a.

These anti-reflective properties and enhanced infrared absorption from multiple scattering facilitates the enhancement in EQE shown in Figure 3b and 4b. Note that that the EQE of the nanowire device was measured at zero bias, corresponding to the higher J_{sc} observed in Figures 3c and 4c, but the overall conversion efficiencies in both the amorphous Si shell and nanocrystalline Si shell devices are lower than the planar devices due to a drop in V_{oc} and FF. A drop in V_{oc} and FF has also been observed in p-n junction nanowire solar cells fabricated from mono-crystalline Si[3,23]. In this case, the drop in Voc and FF can be attributed to a decrease in minority-carrier lifetime caused by faster surface recombination in the nanowire devices than planar devices. Similarly, in a p-i-n thin film Si device architecture, V_{oc} is highly dependent on carrier recombination at the p/intrinsic region interface or within the intrinsic region near this interface[24]. Therefore, the drop in V_{oc} observed in Figure 3c and 4c can be attributed to higher recombination at the p/intrinsic interface due to the high surface area of the core-shell nanowire devices. One method to minimize the drop in V_{oc} is to reduce the surface area by growing sparser nanowires with larger diameter ZnO : Al cores or by growing shorter nanowires. Alternatively, recombination at the p/i interface can be reduced by introducing a thin graded p-type interface layer between the p and intrinsic regions[25].

The lower fill factor of the nanowire device can be attributed to non-conformal coverage of the n⁺ shell, particularly near the base of the nanowires, due to the close proximity of nanowires to each other (Figure 2d). Methods to improve fill factor include tailoring the deposition conditions of the n+, i, and p⁺ Si shell layers for better conformal growth and slightly increasing spacing between nanowires to reduce shadowing effects between nanowires during shell growth. The drop in FF in the nanowire shell devices (Figure 3c and 4c) can also be attributed to high series resistance in the top ZnO : Al contact (particularly for the longer nanowires, l = 800 nm). The high surface area of the nanowires increases the sheet resistance of the top contact, limiting the use of the long nanowires. For example, the top ZnO : Al sheet resistance (without metals grids) increased from 88 Ω/sq. for the planar amorphous Si device to 300 Ω/sq. for the amorphous Si nanowire shell device. Therefore, reducing the resistivity of the top contact would facilitate the use of longer nanowires for further increasing optical absorption. One method to lower the top contact sheet resistance, while maintaining high optical transmission, is to coat the top contact with a network of Ag nanowires[26].

In conclusion, we have incorporated disordered Si nanowires into a core-shell device architecture using two different active shell materials: amorphous Si and nanocrystalline Si. For both devices, the core-shell nanowire devices exhibit low total reflectance leading to enhancement in external quantum efficiency over a wide range of wavelengths compared to a planar control device. As a result, the core-shell nanowire device with amorphous Si absorber shell exhibited a J_{sc} = 13.9 mA/cm² compared to 12.1 mA/cm² of the planar

device. Similarly, the nanowire device with nanocrystalline Si absorber shells showed a J_{sc} of up to 16.6 mA/cm² compared to $J_{sc} = 13.2$ mA/cm² of the planar device. Furthermore, the external quantum efficiency of the nanocrystalline Si nanowire shell solar cell extends the solar spectrum utilization to wavelengths of up to 1000 nm, making it promising as the bottom cell in amorphous Si/nanocrystalline Si tandem radial junction nanowire solar cell. All nanowires and Si shells were grown by conventional large area PECVD methods on glass substrates. Therefore, core-shell nanowire solar cells are an exciting alternate to conventional light trapping techniques (i.e. surface texturing) for large area photovoltaics. Furthermore, the ability to tailor the optical properties of the nanowire device via controlling the nanowire diameter, length, and density makes them attractive for other large area applications such as image sensors for medical imaging and large area photodetectors.

Methods

Silicon nanowire preparation. Si nanowires were grown by the Vapour-Liquid-Solid (VLS) technique[27] in an rf parallel plate PECVD deposition system[10]. These nanowires were grown on Al coated Corning Eagle XG glass substrates. The glass substrates were cleaned, first by immersion in an ultrasonic bath containing acetone and then in one containing isopropyl alcohol. Tin (Sn) nanoclusters, formed by depositing a 2 nm thick Sn film by e-beam evaporation and annealing in vacuum at 400°C for 1 hour, were used as the catalyst for nanowire growth. Nanowires were grown using SiH₄ source gas diluted in H₂ at a pressure of 1400 mTorr and 13.56 Mhz rf plasma density of 16.4 mW/cm². A high H₂ dilution of [H₂]/[SiH₄] = 62 was used to suppress the growth of amorphous Si and improve nanowire growth uniformity. The nanowires were grown at a substrate temperature of 400°C for 15–23 min.

Device preparation. An Al back-contact film was deposited by dc magnetron sputtering and aluminum doped ZnO (ZnO : Al) contacts were deposited by rf magnetron sputtering. The active thin film Si layers were fabricated by rf parallel plate PECVD in a cluster tool deposition system. The device structure was glass/ Al(170 nm)/NWs/ZnO : Al(60 nm)/n⁺/i/p⁺/ZnO : Al(75 nm). The thickness values correspond to those measured on planar substrates. The n⁺ layer thickness was 50 nm and p⁺ layer thickness was 30 nm for all planar devices. Two different intrinsic layers were used: a-Si deposited from SiH₄ source gas and nanocrystalline Si deposited from H₂ diluted SiH₄ gas. The intrinsic amorphous Si layer was prepared using the same conditions using a pressure of 400 mTorr, power density of 7.8 mW/cm² and deposition duration of 30 min. for both the nanowire and planar device. The nanocrystalline Si intrinsic layer was deposited under high pressure (7 Torr), high power density (0.371 W/cm²), conditions that facilitate high deposition rates[28]. The hydrogen dilution ratio was [H₂]/[SiH₄] = 82 which was near the crystalline/amorphous Si transition point. The deposition time of the intrinsic nanocrystalline Si film was 35 min. for nanowire devices and 70 min. for planar devices. Nanocrystalline n⁺ and nanocrystalline p⁺ shells were deposited by H₂ diluted SiH₄ with PH₃ and B₂H₆ dopant gases, respectively. The n⁺ and p⁺ shell thickness were the same for every nanowire device. The deposition times for the Al back contact and ZnO : Al layers were the same for both the core-shell nanowire device and the planar reference device. The deposition time for both the n⁺ and p⁺ nanocrystalline Si shells were longer for the nanowire devices than planar devices to improve nanowire side-wall coverage which was required to achieve efficient charge collection. The resulting nanowire sidewall radial thickness was on average 40 nm for the n⁺ shell and 17 nm for the p⁺ shell, which was determined from SEM images before and after deposition of each shell. Ag gridlines were deposited by e-beam evaporation to lower series resistance of the top ZnO : Al layer. In addition, a drop of conductive Ag paste was placed on the grid line to act as a point of contact for measurement probes. The active area defined by the exposed top ZnO : Al contact was 0.44 cm².

Optical characterization. The total reflectance (including both specular and diffuse components) was measured by a Cary 5000 UV-Vis-NIR spectrophotometer equipped with an integrating sphere. The reflectance was calibrated using Labsphere, Inc. Spectralon Diffuse Reference Standards prior to measurements.

Structural characterization. A Leo 1530 field-emission SEM was used for 45° tilt SEM measurements and a FEI Magellan 400 high-resolution SEM was used for the cross sectional measurement. The cross-sectional sample was prepared using a Zeiss NVision 40 cross-beam instrument to mill a 15 µm long slice at the edge of the sample. Carbon was used as a mask to define the location of the ion-beam cut.

Device characterization. The solar cell devices were characterized by external quantum efficiency (EQE) and current density (*J*)-voltage (*V*) measurements under AM 1.5 global illumination (100 mW/cm²). External quantum efficiency (EQE) measurements, under zero bias conditions, were taken on a PV

Measurements Inc. quantum efficiency system, calibrated using a Si photodiode before measurements. *JV* curves were measured using a Keithley 2400 source meter and solar simulator (ABET Technologies SUN 2000 series) system. A pre-calibrated monocrystalline Si cell was used for calibration. Note that the short-circuit current (J_{sc}) for each device determined from the integrated EQE measurements agreed within 3% to that of the J_{sc} measured by the solar simulator measurements.

1. Tsakalakos, L. *et al*. Silicon Nanowire Solar Cells. *Appl. Phys. Lett.* **91**, 233117–1–3 (2007).
2. Sivakov, V. *et al*. Silicon Nanowire-Based Solar Cells on Glass: Synthesis, Optical Properties, and Cell Parameters. *Nano Lett.* **9**, 1549–1554 (2009).
3. Garnett, E. & Yang, P. Light Trapping in Silicon Nanowire Solar Cells. *Nano Lett.* **10**, 1082–1087 (2010).
4. Li, J. *et al*. Design guidelines of periodic Si nanowire arrays for solar cell application. *Appl. Phys. Lett* **95**, 243111–1–3 (2009).
5. Lin, C. & Povinelli, M. L. Optical Absorption Enhancement in Silicon Nanowire Arrays with a Large Lattice Constant for Photovoltaic Applications. *Opt. Express* **17**, 19371–19381 (2009).
6. Bao, H. & Ruan, X. Optical absorption enhancement in disordered vertical silicon nanowire arrays for photovoltaic applications. *Opt. Letters* **35** (20), 3378–3380 (2010).
7. Lin, C. & Povinelli, M. L. Optimal design of aperiodic, vertical silicon nanowire structures for photovoltaics. *Opt. Express* **19** (S5), A1148–A1154 (2011).
8. Muskens, O. L., Rivas, J. G., Algra, R. E., Bakkers, E. P. & Lagendijk, A. Design of Light Scattering in Nanowire Materials for Photovoltaic Applications. *Nano Lett.* **8**, 2638–2642 (2008).
9. Tsakalakos, L. *et al*. Strong Broadband Optical Absorption in Silicon Nanowire Films. *J. Nanophotonics* **01** (01), 013552 (2007).
10. Adachi, M. M., Anantram, M. P. & Karim, K. S. Optical Properties of Crystalline-Amorphous Core-Shell Silicon Nanowires. *Nano Lett.* **10**, 4093–4098 (2010).
11. Law, M., Greene, L. E., Johnson, J. C., Saykally, R. & Yang, P. Nanowire dye-sensitized solar cells. *Nature Mat.* **4**, 455–459 (2005).
12. Kayes, B. M., Atwater, H. A. & Lewis, N. S. Comparison of the Device Physics Principles of Planar and Radial p-n Junction Nanorod Solar Cells. *J. Appl. Phys.* **97**, 114302–1 (2005).
13. Adachi, M. M. & Karim, K. S. Fabrication of PECVD grown nip silicon nanowire solar cells. *Proc. 35th IEEE Phot. Spec. Conf.* **2010**, 003302–003305 (2010).
14. Kendrick, C. E. *et al*. Radial junction silicon wire array solar cells fabricated by gold-catalyzed vapor-liquid-solid growth. *Appl. Phys. Lett.* **97**, 143108 (2010).
15. Gunawan, O. & Guha, S. Characteristics of Vapor-Liquid-Solid Grown Silicon Nanowire Solar Cells. *Solar Energy Mater. Solar Cells* **93**, 1388–93 (2009).
16. Perraud, S. *et al*. Full process for integrating silicon nanowire arrays into solar cells. *Sol. Energ. Mat. Sol. C.* **93**, 1568–1571 (2009).
17. Kuang, Y. K., van der Welf, K. H. M., Houweling, W. Z. S. & Schropp, R. E. I. Nanorod solar cell with an ultrathin a-Si:H absorber layer. *Appl. Phys. Lett.* **98**, 113111 (2011).
18. Cho, J. *et al*. Sn-catalyzed silicon nanowire solar cells with 4.9% efficiency grown on glass. *Prog. Photovolt: Res. Appl.* doi:10.1002/pip.1245 (2012).
19. Haque, M. S., Naseem, H. A. & Brown, W. D. Interaction of aluminum with hydrogenated amorphous silicon at low temperatures. *J. Appl. Phys.* **78** (8), 3928–3935 (1994).
20. Shah, A., Torres, P., Tscharner, R., Wyrsch, N. & Keppner, H. Photovoltaic Technology: The Case for Thin-Film Solar Cells. *Science* **285**, 692–698 (1999).
21. Rech, R. & Wagner, H. Potential of amorphous silicon for solar cells. *Appl. Phys. A* **69**, 155–167 (1999).
22. Yu, Y., Ferry, V. E., Alivisatos, P. & Cao, L. Dielectric Core–Shell Optical Antennas for Strong Solar Absorption Enhancement. *Nano Lett.* **12**, 3674–3681 (2012).
23. Peng, K. *et al*. Aligned Single-Crystalline Si Nanowire Arrays for Photovoltaic Applications. *Small* **1**, 1062–1067 (2005).
24. Hegedus, S. S., Salzman, N. & Fagen, E. The relation of dark and illuminated diode parameters to the open-circuit voltage of amorphous silicon pin solar cells. *J. Appl. Phys.* **63** (10), 5126–5130 (1988).
25. Arya, R. R., Catalano, A. & Oswald, R. S. Amorphous silicon pin solar cells with graded interface. *Appl. Phys. Lett.* **49**, 1089–1091 (1986).
26. Lee, J. Y., Connor, S. T., Cui, Y. & Peumans, P. Solution-processed metal nanowire mesh transparent electrodes. *Nano Lett.* **8** (2), 689–692 (2008).
27. Wagner, R. S. & Ellis, W. C. Vapor-liquid-solid mechanism of single crystal growth. *Appl. Phys. Lett.* **4** (5), 89 (1964).
28. Rech, B., Roschek, T., Muller, J., Wieder, S. & Wagner, H. Amorphous and microcrystalline silicon solar cells prepared at high deposition rates using RF (13.56 MHz) plasma excitation frequencies. *Sol. Energ. Mat. Sol. C.* **66**, 267–273 (2001).

Acknowledgments

Author contributions

M.M.A. designed, fabricated, and characterized all silicon nanowire devices and control devices under the guidance of K.S.K. and M.P.A. The manuscript was prepared by M.M.A. and all authors contributed in discussing and analyzing the results.

Additional information